



# Capacity and Modeling of Acid Blue 113 Dye Adsorption onto Chitosan Magnetized by Fe<sub>2</sub>O<sub>3</sub> Nanoparticles

Tariq J. Al-Musawi<sup>1</sup> · Nezamaddin Mengelizadeh<sup>2</sup> · Orabi Al Rawi<sup>1</sup> · Davoud Balarak<sup>3</sup>

Accepted: 1 June 2021 / Published online: 7 June 2021

© The Author(s), under exclusive licence to Springer Science+Business Media, LLC, part of Springer Nature 2021

## Abstract

A chitosan polymer was magnetized by coating with magnetite Fe<sub>2</sub>O<sub>3</sub> nanoparticles, and the resultant material (C-Fe<sub>2</sub>O<sub>3</sub>) was first characterized through scanning electron microscopy equipped with energy-dispersive X-ray spectroscopy, transmission electron microscopy, atomic force microscopy, thermogravimetric, X-ray diffractometry, Fourier transform infrared spectroscopy, Brunauer–Emmett–Teller, and point of zero charge analyses. C-Fe<sub>2</sub>O<sub>3</sub> was then employed as a separable and efficient adsorptive agent to remove acid blue 113 (AB113) dye from aqueous solution. The removal efficiency was optimized at different environmental parameter values (pH 3–11, C-Fe<sub>2</sub>O<sub>3</sub> dose: 0.1–1 g/L, initial AB113 dye concentration: 10–100 mg/L, adsorption time: 0–300 min, and temperature: 15–45 °C). Under optimum conditions, an AB113 dye removal efficiency of 99.68% was achieved. In addition, the effect of the presence of NaCl, NaNO<sub>3</sub>, Na<sub>2</sub>CO<sub>3</sub>, and MgSO<sub>4</sub> ions on the AB113 dye removal efficiency could be ranked as NaCl > NaNO<sub>3</sub> > MgSO<sub>4</sub> > Na<sub>2</sub>CO<sub>3</sub>. The statistical analysis using the coefficient of determination, root mean square error, chi-square test, sum of squared errors, and average relative error showed that the Freundlich and pseudo-second-order equations were the best mathematical models for fitting the isothermal and kinetics data. Further kinetics analyses showed that the adsorption of AB113 molecules on C-Fe<sub>2</sub>O<sub>3</sub> active sites was dominated by the intraparticle diffusion process. Thermodynamic parameters indicated that the AB113 dye adsorption process was favorable, endothermic, and spontaneous. Furthermore, an increase in temperature had a positive impact on AB113 dye removal. The regeneration study confirmed the excellent shelf life of C-Fe<sub>2</sub>O<sub>3</sub>, with only a slight loss in the removal efficiency (< 7%) being detected after six operational cycles of AB113 dye adsorption. Compared with other adsorbents, C-Fe<sub>2</sub>O<sub>3</sub> was more effective for the adsorption of AB113 dye, with an adsorption uptake up to 128 mg/g.

---

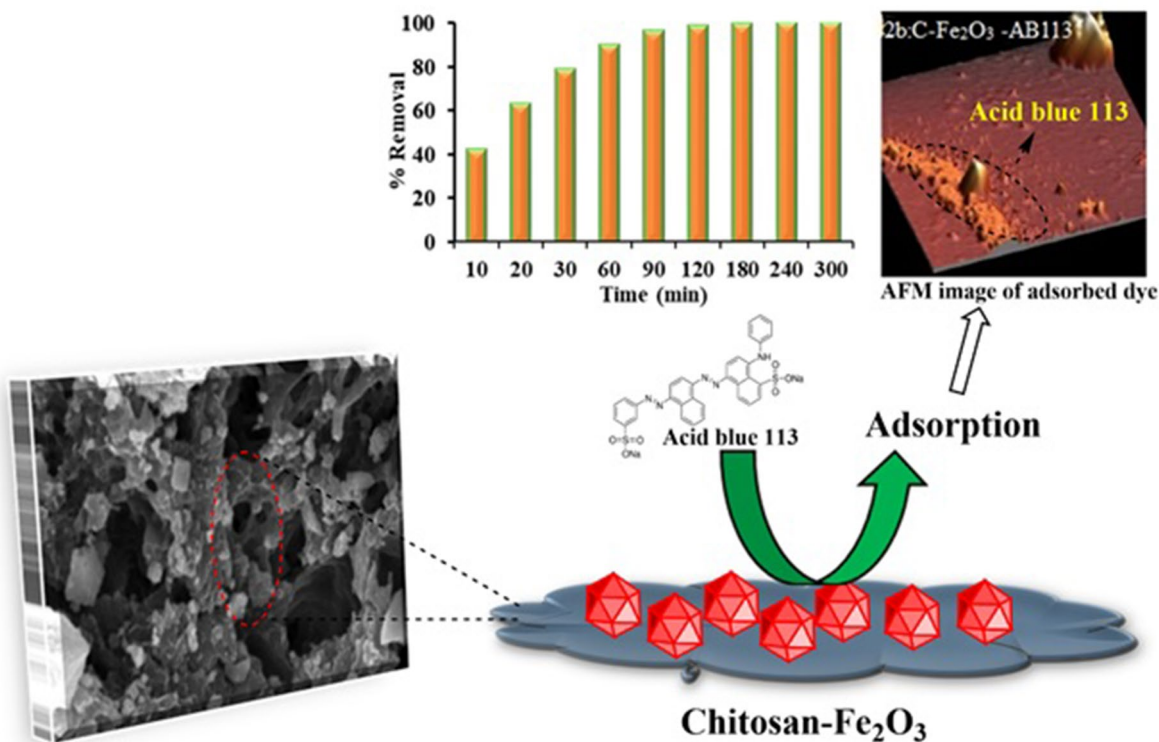
✉ Davoud Balarak  
dbalarak2@gmail.com

<sup>1</sup> Department of Civil Engineering, Faculty of Engineering,  
Isra University, Amman, Jordan

<sup>2</sup> Department of Environmental Health Engineering, Research  
Center of Health, Safety and Environment, Evaz Faculty  
of Health, Larestan University of Medical Sciences, Larestan,  
Iran

<sup>3</sup> Department of Environmental Health, Health Promotion  
Research Center, Zahedan University of Medical Sciences,  
Zahedan, Iran

## Graphic Abstract



**Keywords** Acid blue 113 · Chitosan · Fe<sub>2</sub>O<sub>3</sub> nanoparticles · Modeling · Adsorption capacity

## Introduction

Currently, dye pollutants are among the most dangerous compounds that are pumped into the environment via the effluents of different factories, such as those for paper, textiles, paints, leather, plastic, and cosmetics [1, 2]. Azo dyes are widely applied in various dyeing processes due to their high activity; thus, these types of dyes generally make up approximately 50–70% of the total dye quantity employed in textile, plastic, and paper industries [3–5]. On the other hand, simple azo dyes (e.g., picric acid and anionic and cationic dyes) consist of hydroxyl groups in their structure and do not establish a strong bond with the texture of fabrics and linen fibers; thus, for dyeing, a large quantity of simple azo dyes are consumed [6, 7]. Azo dyes contain natural and synthetic organic compounds and are characterized in nature as refractory and stable organic pollutants [8–10]. For example, acid blue 113 (AB113) dye has been selected as the target dye due to its wide application in industry, especially in the paints and textile industries. Furthermore, studies have shown that azo dyes have two types of auxochrome (–OH, –NH<sub>2</sub>, and NR<sub>2</sub>) and chromophore (C=C, N=N, and C=O) functional groups [11, 12]. These two groups have a high

tendency to attach to benzene and naphthalene rings that may be found in wastewater and, in some cases, can also be attached to aliphatic and heterocyclic groups, leading to the generation of hazardous byproducts [13–15]. In addition to their toxicity to humans, the presence of dyes in water bodies can disturb aquatic life via their ability to reduce the penetration of sunlight, which is essential for photosynthesis [16, 17]. Thus, wastewater containing dyes must go through efficient purification processes prior to discharge to the environment. In reality, dyes cannot be lowered to the acceptable concentration via pretreatment or conventional methods [6, 11]. Therefore, researchers are looking for advanced techniques to effectively remove these compounds prior to discharge into water bodies [1, 18].

Low portions of dye pollutants are removed by conventional treatment methods. Furthermore, some efficient methods have high costs [11, 17]. Therefore, alternative techniques to traditional dye removal methods are still in demand. Currently, the efficient and low-cost method used for this purpose is separation by adsorption processes [19–21]. One of the most important operational and economic factors of adsorption treatment is the adsorbent used, as well as separating the spent adsorbents after treatment.

To solve the separation problem and simultaneously increase the adsorption efficiency of the used adsorbent, the magnetization of used adsorbents is a promising method [20]. Coating used adsorbents with magnetic nanoparticles has also been recommended because this modification method not only improves the removal efficiency but also improves the economic efficiency, environmental compatibility, mechanical strength, reusability and scalability of the magnetized adsorbents [22, 23]. In this direction,  $\text{Fe}_2\text{O}_3$  nanoparticles have been widely used [24, 25]. However, the use of pure magnetic particles also has a drawback, as these particles have a high tendency to agglomerate in aqueous solution. When these particles are combined with other materials, such as chitosan, the agglomeration mechanism is hampered [26].

Natural materials are welcomed and highly recommended for application as adsorptive treatment agents [27]. Chitosan is a natural hydrophilic and cationic biopolymer obtained by the removal of acetyl-chitin groups in an alkaline environment and has been extensively studied as an adsorbent to remove a variety of contaminants (e.g., heavy metals, antibiotics, and dyes) [27, 28]. Chitosan has low cytotoxicity and unique chemical properties; furthermore, chitosan is obtained from chitin, which is effortlessly attained from shrimp and crab shells (these are considered waste products of the seafood industry) [27]. Chitosan has two hydroxyl groups and one amino group in the glycosidic fraction and has a suitable matrix that allows fabrication with foreign particles [22]. Because chitosan dissolves in acidic and aqueous solutions, there is no need to use hazardous organic solvents [21, 29]. Sun et al. used a chitosan/cellulose composite to adsorb lead ions from aqueous solutions [30]. Furthermore, chitosan magnetized by  $\text{Fe}_2\text{O}_3$  nanoparticles has also been employed for eradicating heavy metals from solutions [31, 32].

Through our review of previous research, it was found that very few studies have been performed on the removal of organic pollutants, such as dyes using chitosan magnetized by  $\text{Fe}_2\text{O}_3$  nanoparticles (hereafter referred to as C- $\text{Fe}_2\text{O}_3$ ). In addition, studies on the removal of AB113 dye by C- $\text{Fe}_2\text{O}_3$  based adsorption process have not yet been reported. Therefore, the present study offers a comprehensive account of the application of C- $\text{Fe}_2\text{O}_3$  as an efficient and recyclable adsorbent for the removal of AB113 dye from aqueous solutions. Initially, the surface and structural characterizations of used C- $\text{Fe}_2\text{O}_3$  are obtained by advanced characterization analyses. The adsorption process of the AB113 dye and C- $\text{Fe}_2\text{O}_3$  couple is reported with different environmental parameters. Isotherm and kinetics studies, which are the focus of this study, are conducted using linear and nonlinear models. The thermodynamics parameters are also determined. Finally, the recyclability of C- $\text{Fe}_2\text{O}_3$  is evaluated in several AB113 dye adsorption–desorption cycles.

## Materials and Methods

### Materials

Chitosan with a chemical formula  $(\text{C}_6\text{H}_{11}\text{O}_4\text{N})_n$  and purity of 98% was purchased from Sigma-Aldrich (Germany). Acetic acid ( $\geq 99.7\%$ ),  $\text{FeCl}_3 \cdot 6\text{H}_2\text{O}$  ( $\geq 98\%$ ),  $\text{FeCl}_2 \cdot 4\text{H}_2\text{O}$  ( $\geq 99\%$ ), HCl (36.5%), and NaOH ( $\geq 98\%$ ) were purchased from Merck (Germany). In addition, a stock solution of AB113 dye (purity  $> 98\%$ ) was bought from the Alvan Sabet factory (Hamadan, Iran).

### Preparation of C- $\text{Fe}_2\text{O}_3$

Initially, 2 g of chitosan was gradually dissolved in deionized water (100 mL) containing 2% acetic acid and magnetically stirred at 120 rpm for 1 h. To ensure the dissolution of all used chitosan quantities, the prepared chitosan solution was homogenized by means of ultrasonic waves for 20 min using an ultrasonic device (Sunshine ultrasonic cleaner, model SS6508T). A mixture of  $\text{FeCl}_3 \cdot 6\text{H}_2\text{O}$  (6.1 g) with  $\text{FeCl}_2 \cdot 4\text{H}_2\text{O}$  (4.2 g) at a molar ratio of 2:1 was mixed with the chitosan solution with the simultaneous dropwise addition of a 30% NaOH solution (this process was carried out through the employment of a nitrogen gas stream at a temperature  $\geq 70$  °C, while being mixed at 1000 rpm for 2 h). Subsequently, the mixture was homogenized by ultrasonic waves for 20 min. After that, the temperature of the homogenized mixture was increased to 90 °C, and when reaching this temperature, the stirring process was further continued for 2 h. Next, the resulting mixture was deoxygenated 4 times with distilled water and rinsed with ethanol. The supernatant (C- $\text{Fe}_2\text{O}_3$ ) was then collected in a container and neutralized. Afterward, a centrifuge (3600 rpm for 10 min) was used to separate C- $\text{Fe}_2\text{O}_3$  from the solution, followed by drying in an oven (70 °C for 5 h). Eventually, after crushing and crystallization, C- $\text{Fe}_2\text{O}_3$  was placed in a desiccator in the presence of a magnetic field for dehumidification.

### Characterization Analyses

Surface and structural characterizations of the C- $\text{Fe}_2\text{O}_3$  sample were performed using XRD with a Cu K $\alpha$  radiation source (ESCALAB250 Thermo Fisher), SEM (Model JSM6510LV, JEOL Ltd., Tokyo, Japan) connected with an EDX spectroscopy, TEM (Philips CM120, Netherlands), FTIR spectroscopy (PerkinElmer, Spectrum GX), and UV–Vis spectrophotometry (DR5000, HACH). The magnetization curves of  $\text{Fe}_2\text{O}_3$  nanoparticles and C- $\text{Fe}_2\text{O}_3$  were measured using a vibrating sample magnetometer (Lake Shore Cryotronics, 7407-S) at ambient temperature [33]. The improvement in the thermal stability of chitosan after

magnetization with  $\text{Fe}_2\text{O}_3$  nanoparticles was determined using thermogravimetric analysis (TGA, TA Instruments SDT Q600, USA). The surface area and pore size were obtained by employing Brunauer–Emmett–Teller (BET) analyses [34]. The changes in the topography of the C- $\text{Fe}_2\text{O}_3$  surface due to AB113 dye adsorption were explored using atomic force microscopy (AFM, Nano Wizard II, JPK Germany). The  $\text{pH}_{\text{pzc}}$  value of C- $\text{Fe}_2\text{O}_3$  was evaluated using a previously reported methodology [35].

## Batch Experiments

The AB113 dye adsorption experiments were carried out in several 200 mL Erlenmeyer flasks with a dye solution of 100 mL. AB113 dye removal by C- $\text{Fe}_2\text{O}_3$  was optimized by varying the pH (3–11), C- $\text{Fe}_2\text{O}_3$  dose (0.1–1 g/L), initial AB113 dye concentration (10–100 mg/L), adsorption time (0–300 min), and temperature (15–45 °C). It is worth mentioning that the temperature of the working solutions was controlled using a thermostated water bath (model: Grant GLS5400, England). In addition, the effect of the presence of interference ions ( $\text{NaCl}$ ,  $\text{NaNO}_3$ ,  $\text{Na}_2\text{CO}_3$ , and  $\text{MgSO}_4$ ) on the adsorptive performance of C- $\text{Fe}_2\text{O}_3$  was examined. All

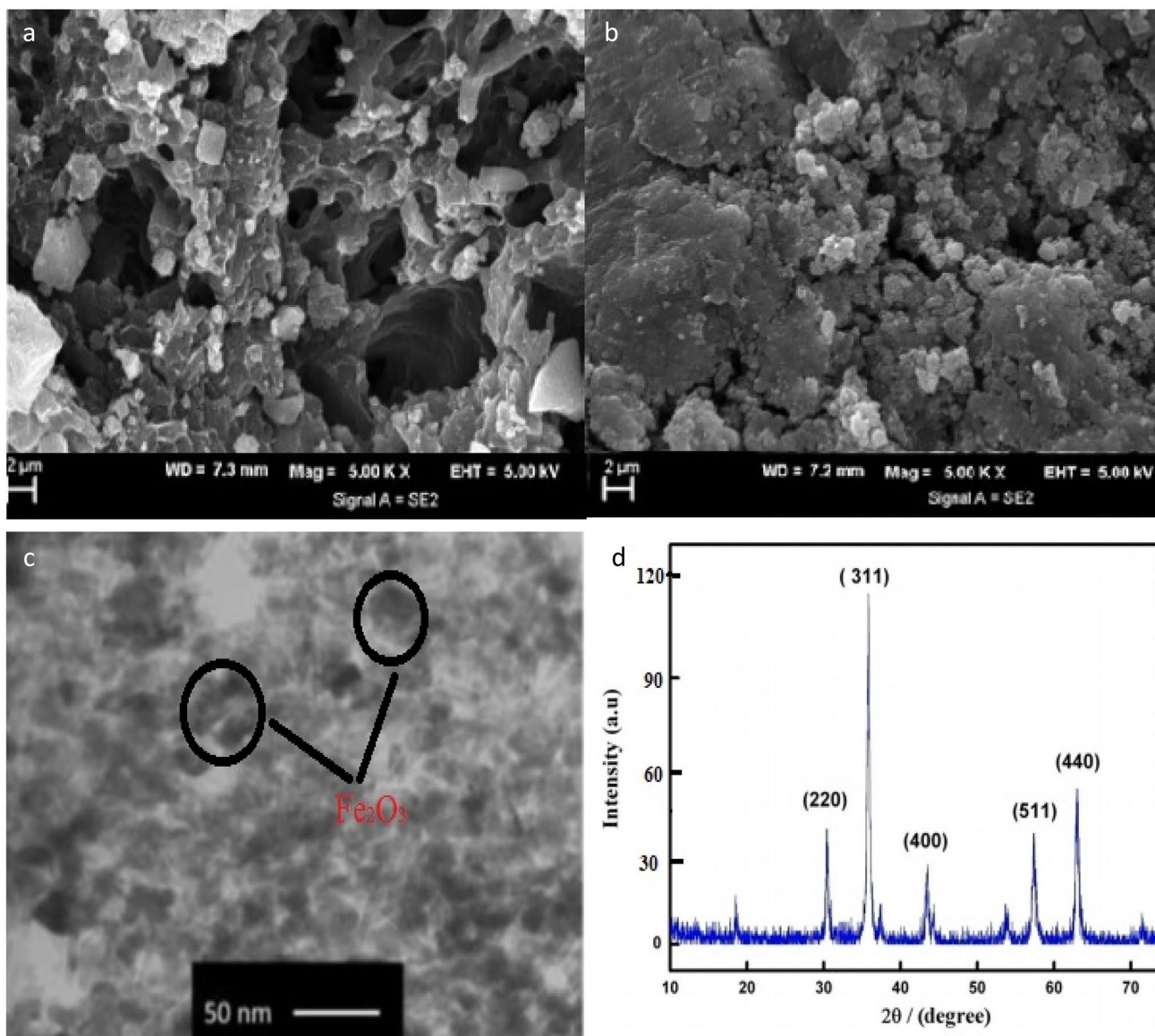


**Fig. 1** SEM images of C- $\text{Fe}_2\text{O}_3$  before (a) and after (b) AB113 dye adsorption. TEM image of C- $\text{Fe}_2\text{O}_3$  (c). X-ray diffraction pattern of C- $\text{Fe}_2\text{O}_3$  (d)



flasks were placed in a shaker incubator at 120 rpm. Except for the thermodynamic experiments, which were performed from 288 to 318 K, the flasks were maintained at room temperature ( $25 \pm 2$  °C) throughout the adsorption experiments. For the kinetic study, the experimental data of the analysis of the effects of the initial AB113 dye concentration on the C-Fe<sub>2</sub>O<sub>3</sub> adsorption capacity were used. Furthermore, for the isotherm study, an experiment was conducted to determine the relationship between the adsorption capacity of C-Fe<sub>2</sub>O<sub>3</sub> at equilibrium and the AB113 dye concentration. During the adsorption process, a 3 mL liquid sample was taken from each flask at regular adsorption time intervals and subjected to centrifugation at  $1509 \times g$  for 15 min. The concentration of AB113 dye in the separated supernatant was determined using a UV–Vis laboratory spectrophotometer (DR 5000, HACH) at  $\lambda_{\text{max}} = 560$  nm. From the determined AB113 dye concentrations, the dye removal efficiency ( $R$  (%)) and adsorption capacity (or uptake) ( $q_t$ ) of C-Fe<sub>2</sub>O<sub>3</sub> for AB113

dye were calculated using Eqs. (1) and (2), respectively [36, 37].

$$RE(\%) = \frac{(C_0 - C_t)}{C_0} \times 100 \quad (1)$$

$$q_t = \frac{(C_0 - C_t)}{M/V} \quad (2)$$

where  $C_0$  is the initial AB113 dye concentration (mg/L),  $C_t$  is the AB113 dye concentration after a specific time of the adsorption process ( $t$ , min),  $M$  is the C-Fe<sub>2</sub>O<sub>3</sub> mass (g), and  $V$  is the volume of the AB113 dye solution (L) (100 mL). Note that the AB113 dye concentration and C-Fe<sub>2</sub>O<sub>3</sub> adsorption capacity at equilibrium time are denoted in Eq. (1) by  $C_e$  (mg/L) and  $q_e$  (mg/g), respectively.

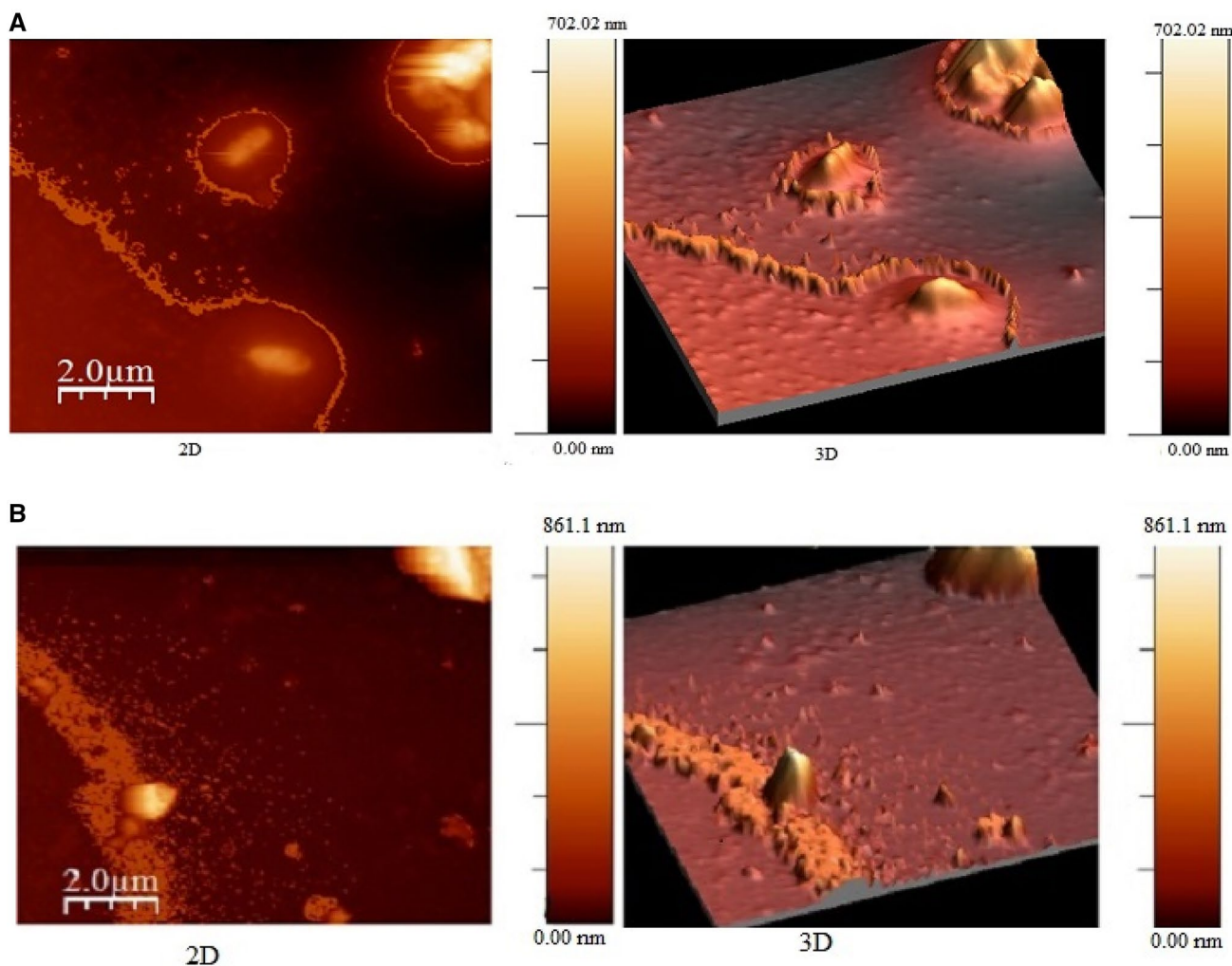


**Fig. 2** 2D and 3D AFM images of C-Fe<sub>2</sub>O<sub>3</sub> before (A) and after (B) adsorption of AB113 dye

### Error Function Analysis

The purpose of conducting the error function analysis in the present study is to assess the compatibility of the theoretical isotherm and kinetics model with the

experimental data. However, the experimental data were fitted with both linear and nonlinear equations of these models. Depending on the values of the coefficient of determination ( $R^2$ ), sum of squared errors ( $SSE$ ) (Eq. 3), root mean square error ( $RMSE$ ) (Eq. 4), chi-square test ( $\chi^2$ )

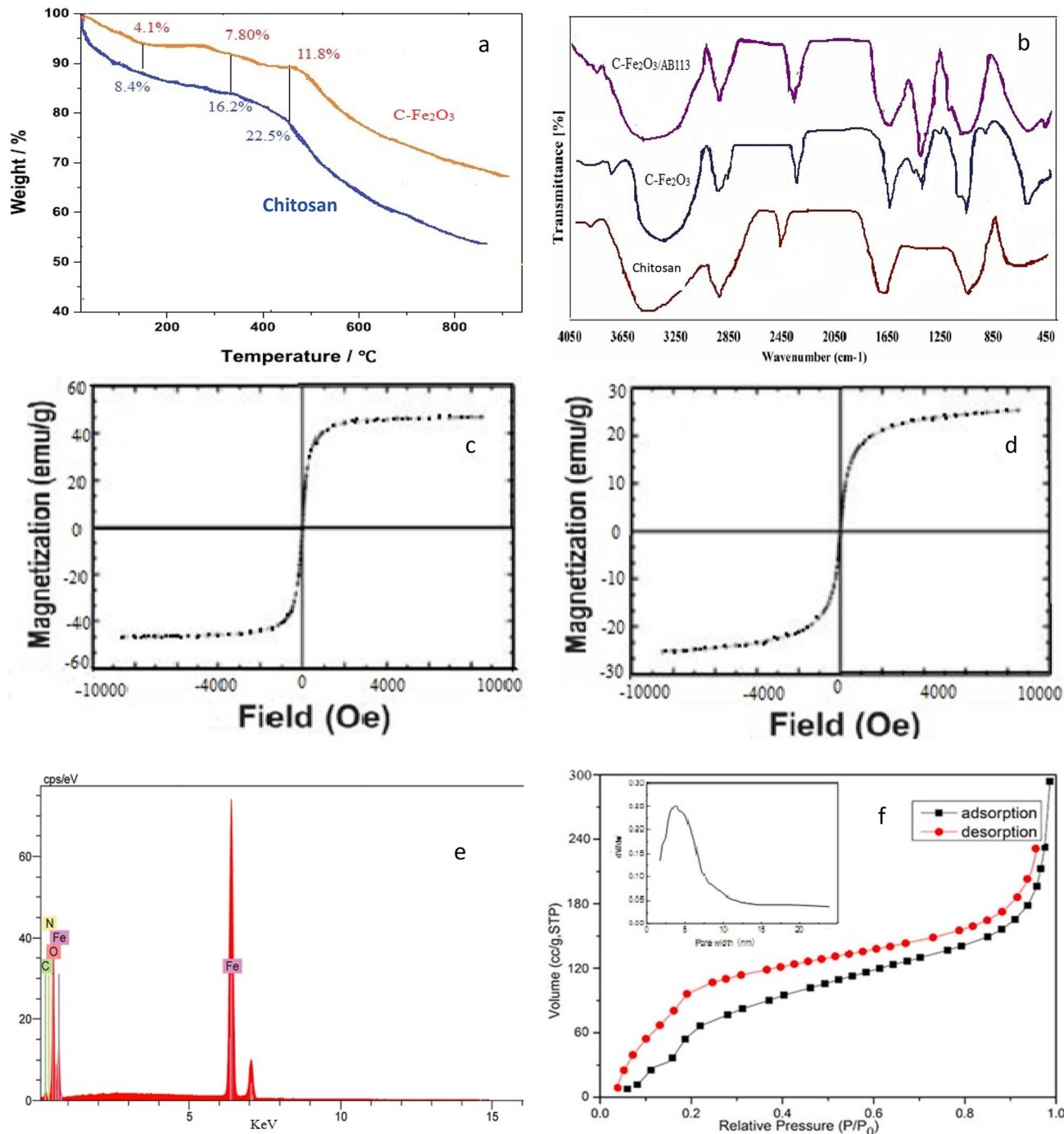


**Fig. 3** TGA graph of chitosan and C-Fe<sub>2</sub>O<sub>3</sub> (a). FTIR spectra of chitosan, C-Fe<sub>2</sub>O<sub>3</sub> before and C-Fe<sub>2</sub>O<sub>3</sub> after reaction with the AB113 dye (C-Fe<sub>2</sub>O<sub>3</sub>/AB113) (b). Magnetization curves of the Fe<sub>2</sub>O<sub>3</sub>

nanoparticles (c) and C-Fe<sub>2</sub>O<sub>3</sub> (d). EDX spectrum of C-Fe<sub>2</sub>O<sub>3</sub> (e). N<sub>2</sub> adsorption–desorption isotherms and pore size analyses of the C-Fe<sub>2</sub>O<sub>3</sub> (f)

(Eq. 5), and average relative error (*ARE*) (Eq. 6), the most appropriate model for the experimental data was evaluated [38, 39].

$$\text{sum of squared errors (SSE)} = \sum_{i=1}^n (q_{\text{exp}} - q_{\text{ecal}})^2 \quad (3)$$

$$\text{root mean square error (RMSE)} = \sqrt{\frac{1}{n-p} \sum_{i=1}^n (q_{\text{exp}} - q_{\text{ecal}})^2} \quad (4)$$

$$\text{chi-square test } (x^2) = \sum_{i=1}^n \left[ \frac{(q_{\text{exp}} - q_{\text{ecal}})^2}{q_{\text{ecal}}} \right] \quad (5)$$

$$\text{average relative error (ARE)} = \frac{100}{n} \sum_{i=1}^n \left[ \frac{q_{\text{exp}} - q_{\text{ecal}}}{q_{\text{exp}}} \right] \quad (6)$$

where  $q_{\text{exp}}$  is the experimental uptake determined based on Eq. (2), and  $q_{\text{ecal}}$  is the calculated uptake determined from the application of the relevant model with the experimental data.

## Results and Discussion

### Characterization Analyses

The SEM images of the C-Fe<sub>2</sub>O<sub>3</sub> before and after AB113 dye adsorption are shown in Fig. 1a and 1b, respectively. It appears that C-Fe<sub>2</sub>O<sub>3</sub> exhibits an extremely rough surface and porous structure, and many fragments are randomly spread onto this material (Fig. 1a). In reality, these morphological characterizations of C-Fe<sub>2</sub>O<sub>3</sub> indicate that this adsorbent has a large reaction area for adhering AB113 dye molecules. After AB113 dye adsorption (Fig. 1b), the surface and pores of C-Fe<sub>2</sub>O<sub>3</sub> are completely covered, which provides an indication about the ability of C-Fe<sub>2</sub>O<sub>3</sub> to adsorb AB113 dye molecules.

Figure 1c is a TEM image of the C-Fe<sub>2</sub>O<sub>3</sub> sample taken at a scale of 50 nm. From this figure, it is perceived that the Fe<sub>2</sub>O<sub>3</sub> nanoparticles are entrenched into the chitosan structure, where the light-colored area belongs to chitosan and the dark spots represent the Fe<sub>2</sub>O<sub>3</sub> nanoparticles. Furthermore, the TEM image reveals that the synthesized C-Fe<sub>2</sub>O<sub>3</sub> particles are almost spherical in shape, and no aggregation is observed between these particles. The size of the C-Fe<sub>2</sub>O<sub>3</sub> particles is approximately 50 nm, as also confirmed by XRD.

The X-ray diffraction pattern of C-Fe<sub>2</sub>O<sub>3</sub> is depicted in Fig. 1d. The C-Fe<sub>2</sub>O<sub>3</sub> has major peaks at  $2\theta = 63^\circ$  and  $36^\circ$ . The average size of C-Fe<sub>2</sub>O<sub>3</sub> is calculated by substituting the main peak phase value of the C-Fe<sub>2</sub>O<sub>3</sub> in the Scherrer

formula (Eq. 7). Based on this equation, the synthesized nanoparticle size in the main peak at  $2\theta = 36^\circ$  (with an intensity of approximately 120 a.u.) is determined to be 35.5 nm.

$$D = \frac{K\lambda}{\beta \cos\theta} \quad (7)$$

where  $D$  is the mean size of C-Fe<sub>2</sub>O<sub>3</sub>,  $K$  is a fixed number equal to 0.89,  $\lambda$  is the wavelength of the Cu-K $\alpha$  radiation (nm),  $\beta$  is the width of the main peak at half its intensity (radians) and  $\theta$  (diffraction angle, radians) is the peak position in the XRD pattern [40].

Figure 2 shows the 2D and 3D AFM images, which are used to compare the topographical changes on the C-Fe<sub>2</sub>O<sub>3</sub> surface as a result of AB113 dye adsorption. Before adsorption (Fig. 2A), the C-Fe<sub>2</sub>O<sub>3</sub> topography is characterized by many scattered bumps and small masses. It is clear that these masses cluster around large blocks, which may be due to the Fe<sub>2</sub>O<sub>3</sub> nanoparticles attracting them. However, in Fig. 2B, it can be seen that after AB113 dye adsorption, remarkable changes occur in the surface topography of C-Fe<sub>2</sub>O<sub>3</sub>. The previously diagnosed bumps are completely covered, and more masses are dispersed onto the C-Fe<sub>2</sub>O<sub>3</sub> surface, which denotes the existence of AB113 dye molecules on the C-Fe<sub>2</sub>O<sub>3</sub> surface. Similar results relevant to the AFM analysis in the present study have been presented in previous works [23, 24].

The TGA graph of chitosan and C-Fe<sub>2</sub>O<sub>3</sub> is presented in Fig. 3a. The first weight loss detected up to 130 °C is related to the dehydration of water molecules from all the chitosan and C-Fe<sub>2</sub>O<sub>3</sub>. The second thermal step occurs in the temperature range of 130–320 °C. The further dehydration, depolymerization, and acetylation process of chitosan, which often occurs at this temperature range, can be the reason for the detected weight loss. The third step is observed at temperatures > 320 °C. The weight loss at this step is ascribed to thermal decomposition in the chitosan structure at high temperatures. These thermal steps have also been reported in other studies [22, 27]. In the case of C-Fe<sub>2</sub>O<sub>3</sub>, decomposition and weight loss are observed at higher temperatures compared to chitosan, which indicates an improvement in the thermal stability of chitosan by the incorporation of Fe<sub>2</sub>O<sub>3</sub> nanoparticles; this has also been reported by other studies [27].

The FTIR spectra of chitosan (C), C-Fe<sub>2</sub>O<sub>3</sub>, and C-Fe<sub>2</sub>O<sub>3</sub> after reaction with AB113 dye (C-Fe<sub>2</sub>O<sub>3</sub>/AB113) samples are shown in Fig. 3b. In the chitosan spectrum, peaks related to C–H, N–H, and C–O–C bands are observed at 2875 cm<sup>-1</sup>, 1650 cm<sup>-1</sup>, and 1066 cm<sup>-1</sup>, respectively. All of the above peaks can be detected in the spectrum of C-Fe<sub>2</sub>O<sub>3</sub>. Peaks at 1570 cm<sup>-1</sup> and 1260 cm<sup>-1</sup> are observed, and the peak at 2420 cm<sup>-1</sup> in chitosan becomes the larger peak at 2340 cm<sup>-1</sup> in C-Fe<sub>2</sub>O<sub>3</sub>. The resulting changes in the spectrum of

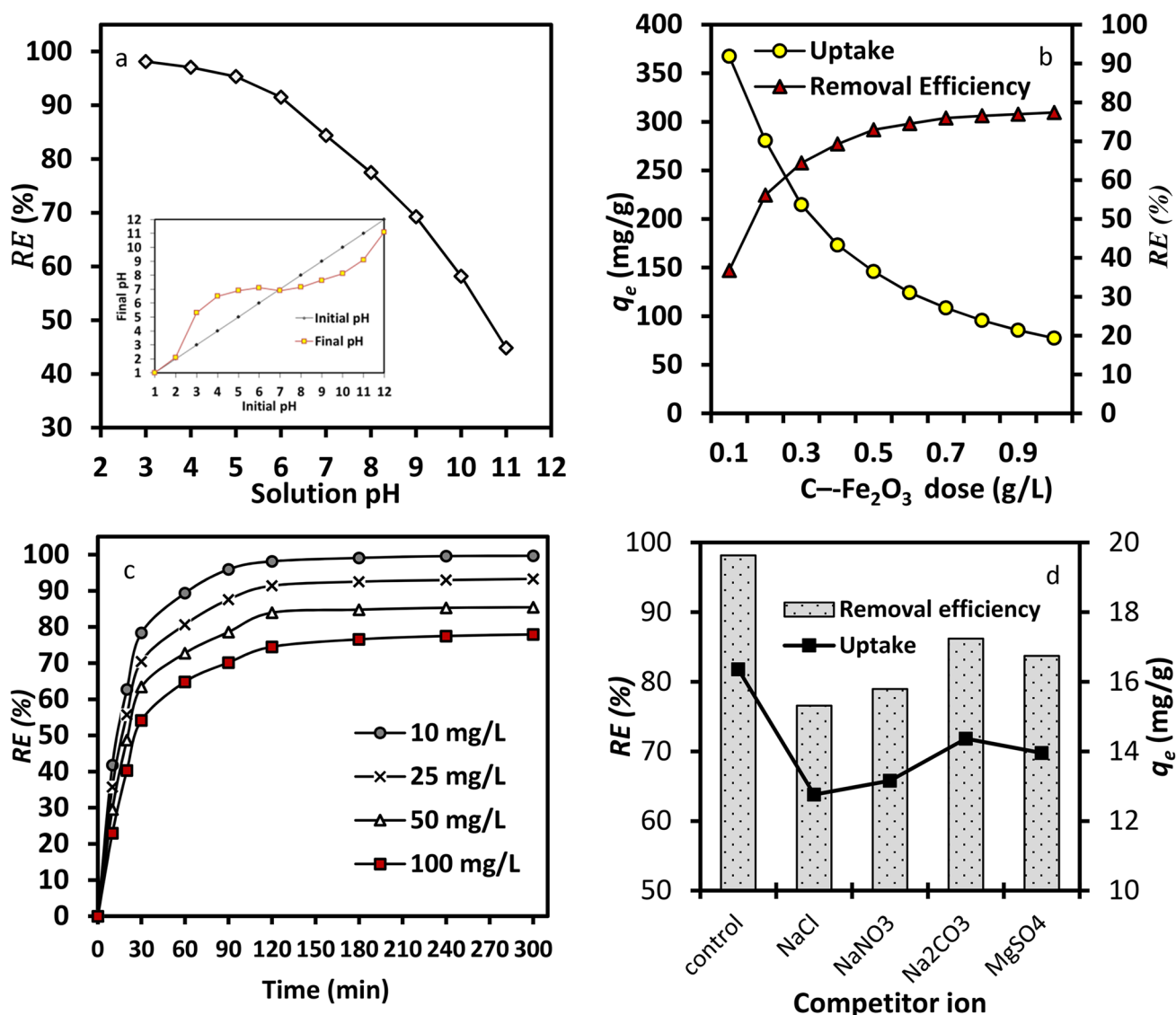


**Fig. 4** Effect study of pH and the  $pH_{pzc}$  analysis (a), C-Fe<sub>2</sub>O<sub>3</sub> dose (b), Initial Ab113 dye concentration (c), and Interference ions (d)

C-Fe<sub>2</sub>O<sub>3</sub> indicate the combination of Fe<sub>3</sub>O<sub>4</sub> with chitosan [27]. Additionally, the peak of the Fe–O band can be spotted at 590 cm<sup>-1</sup>, which indicates the existence of magnetite Fe<sub>2</sub>O<sub>3</sub> nanoparticles in the produced samples.

The magnetization curves of chitosan and C-Fe<sub>2</sub>O<sub>3</sub> provided by the VSM analysis are presented in Fig. 3c and d, respectively. From this figure, the saturation magnetization value of C-Fe<sub>2</sub>O<sub>3</sub> is 24.5 emu/g, which shows a 46% reduction in magnetization compared to 45.5 emu/g for Fe<sub>3</sub>O<sub>4</sub> nanoparticles. This decrease in magnetic properties is due to the fabrication of chitosan with Fe<sub>3</sub>O<sub>4</sub> magnetic nanoparticles; thus, this material can be separated from aqueous solutions using a magnet [23]. Notably, C-Fe<sub>2</sub>O<sub>3</sub> is a highly magnetic material, despite containing nonmagnetic chitosan [26]. Based on the VSM analysis, the superparamagnetic

structure of the Fe<sub>3</sub>O<sub>4</sub> nanoparticles is confirmed in the present study. The absence of a residual loop in the VSM diagram indicates the supermagnetic behavior of the Fe<sub>3</sub>O<sub>4</sub> nanoparticles, although the interaction with chitosan leads to a decrease in their intensity [27, 41].

The EDX analysis (Fig. 3e) performed on the C-Fe<sub>2</sub>O<sub>3</sub> sample shows the presence of C (3.44%), N (1.02%), O (23.94%), and Fe (71.6%). C and N are essential elements in the structure of chitosan [21, 22]. On the other hand, the presence of Fe and O in the structure of C-Fe<sub>2</sub>O<sub>3</sub> is the result of the successful magnetizing process of chitosan by Fe<sub>2</sub>O<sub>3</sub> nanoparticles.

BET analysis (Fig. 3f) revealed that the surface area of C-Fe<sub>2</sub>O<sub>3</sub> is 112.9 m<sup>2</sup>/g. In addition, the pore volume and mean diameter are 0.345 cm<sup>3</sup>/g and 17.2 nm, respectively.



Compared with the documented surface area and pore volume values for a sample of pure chitosan (91.4 m<sup>2</sup>/g and 0.285 cm<sup>3</sup>/g) [27], it can be concluded that the coating of chitosan with Fe<sub>2</sub>O<sub>3</sub> significantly enhances the characterization properties of this polymer. Notably, solid materials with a large surface area are favorable as adsorbents in adsorption treatment systems, as this parameter reflects the number of adsorption sites for pollutant molecules. In addition, the pore size of C-Fe<sub>2</sub>O<sub>3</sub> is within the range of 2–50 nm; thus basically it is classified as a mesoporous material based on IUPAC definition [42].

### Effects of the Environmental Parameters on AB113 Dye Adsorption

Several adsorption studies have demonstrated that the adsorption process of organic pollutants is significantly affected by various environmental parameters [43–45]. Generally, the solution pH and temperature have a considerable effect on the adsorption process, as the ionization degree of the adsorbent surface and the dissolution rate of the organic pollutant molecules mainly depend on these two parameters. From an economic perspective and for designing large-scale adsorption treatment systems, the determination of the optimum adsorbent dose for the removal of pollutants is considered a key factor for such studies. Furthermore, the most important analyses in the isotherm study depend on the relationship between the equilibrium uptakes of the adsorbent for the target pollutant at a constant temperature. Investigation of the effects of adsorption time at different initial pollutant concentrations is essential for kinetic studies. Additionally, Samarghandi et al. [46] reported that the presence of some ions in aqueous solution may compete with the absorption of the target pollutant. In the present work, the effects of the abovementioned environmental parameters on AB113 dye adsorption and removal efficiency were studied, and the results are depicted in Fig. 4. Moreover, the temperature effect data are presented in the thermodynamic study.

#### Solution pH

The solution pH of the solution greatly affects the rate of adsorption; under acidic conditions, the adsorbent surface becomes protonated and has a more positive charge. This charge causes an electrostatic interaction between the adsorbent and negatively charged ions in the water. Conversely, in an alkaline state, the adsorbent surface becomes negatively charged, and the interaction between the adsorbent and the positive ions increase [39]. In the present study, the effect of solution pH on the removal efficiency of AB113 dye by C-Fe<sub>2</sub>O<sub>3</sub> was investigated from pH 3 to 11, and the results are depicted in Fig. 4a (AB113 dye concentration: 10 mg/L, adsorption time: 120 min, and C-Fe<sub>2</sub>O<sub>3</sub> dose: 0.6 g/L). As

seen, with an increasing pH, the dye adsorption efficiency decreases significantly. At low pH values, more protons exist, so the amine groups in chitosan are protonated; thus, the electrostatic force between the negatively charged dye molecules and the positively charged adsorbent sites increases and more adsorption occurs [27]. Additionally, the high adsorption under acidic conditions can be explained by a p*H*<sub>pzc</sub> analysis. In the present study, the p*H*<sub>pzc</sub> of C-Fe<sub>2</sub>O<sub>3</sub> is determined to be approximately 7 (inset picture in Fig. 4a). Based on this, at solution pH values greater than 7, the surface of C-Fe<sub>2</sub>O<sub>3</sub> is negatively charged, while for pH values lower than 7, the surface has a positive charge [40]. In contrast, the AB113 dye molecule (having two sulfonated (–SO<sub>3</sub><sup>–</sup>) groups) is a disulfonate acid dye (with a p*K*<sub>a</sub> of 0.5), and at pH values higher than 0.5, AB113 tends to have a negative charge. Thus, under acidic conditions, increasing the density of positive charges on the C-Fe<sub>2</sub>O<sub>3</sub> surface may be behind the enhanced AB113 dye removal. At higher pH values, OH<sup>–</sup> in the environment competes with the studied pollutant for combining with chitosan, thus reducing the adsorption rate of AB113 dye on the cationic adsorbent [4].

#### C-Fe<sub>2</sub>O<sub>3</sub> dose

The effect of the C-Fe<sub>2</sub>O<sub>3</sub> dose was investigated by varying the dose from 0.1 g/L to 1 g/L with the following experimental conditions: initial concentration of AB113 dye = 10 mg/L, pH 3, and adsorption time: 120 min. As shown in Fig. 8, it is revealed that with an increasing quantity of C-Fe<sub>2</sub>O<sub>3</sub>, the removal efficiency also increases. This result is because of the increase in total surface area by increasing the C-Fe<sub>2</sub>O<sub>3</sub> dose, which in turn increases the availability of active adsorption sites for AB113 adsorption [47]. The maximum adsorption of AB113 is observed at 0.6 g/L with an adsorption capacity of 124.2 mg/g for C-Fe<sub>2</sub>O<sub>3</sub>. Therefore, a dose of 0.6 g/L was selected for further batch experiments. Notably, the removal of AB113 dye onto C-Fe<sub>2</sub>O<sub>3</sub> is found to be constant with an increasing dose. The reduction in AB113 dye removal with a further increase in the adsorbent dose might be due to a decrease in the available sites and surface area and due to the agglomeration of C-Fe<sub>2</sub>O<sub>3</sub> particles that occurs at high doses [48]. The results of this experiment are in accordance with the results of previous studies [49].

#### AB113 Dye Concentration and Contact Time

Figure 4c shows the kinetics curves, which represent the removal efficiency of AB113 dye as a function of adsorption time (0–300 min) with different concentrations (10–100 mg/L). The other parameters were fixed as the following: pH 3 and C-Fe<sub>2</sub>O<sub>3</sub> dose = 0.6 g/L. The plotted curves of Fig. 4c present similar profiles at all analyzed concentrations of AB113 dye. These curves show a very

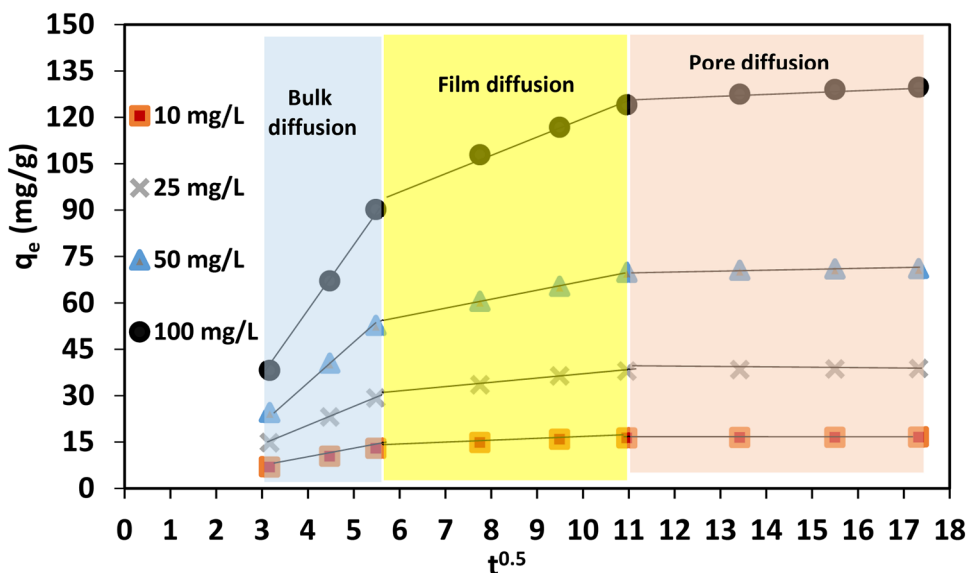
**Table 1** Results of the kinetic analyses of AB113 dye adsorption on C-Fe<sub>2</sub>O<sub>3</sub>

<i>C</i> <sub>0</sub> (mg/L)	<i>q</i> <sub>e</sub> (exp))	PFO kinetics model						
		<i>q</i> <sub>e</sub> (cal)	<i>K</i> <sub>1</sub>	<i>R</i> <sup>2</sup>	<i>x</i> <sup>2</sup>	<i>RMSE</i>	<i>SSE</i>	<i>ARE</i>
10	16.61	9.24	0.026	0.977	11.20	17.10	9.25	13.84
25	38.86	21.18	0.023	0.975	13.95	11.84	9.38	13.02
50	71.21	42.84	0.022	0.969	14.48	11.95	18.41	9.28
100	129.80	11.71	0.021	0.978	8.46	6.45	4.71	8.73
<i>C</i> <sub>0</sub> (mg/L)	<i>q</i> <sub>e</sub> (exp))	PSO kinetics model						
		<i>q</i> <sub>e</sub> (cal)	<i>K</i> <sub>2</sub>	<i>R</i> <sup>2</sup>	<i>x</i> <sup>2</sup>	<i>RMSE</i>	<i>SSE</i>	<i>ARE</i>
10	16.61	17.36	0.0053	0.999	1.48	2.15	1.09	2.71
25	38.86	40.98	0.0018	0.999	1.76	2.95	1.49	3.11
50	71.21	75.75	0.0008	0.998	2.35	1.79	4.18	1.48
100	129.80	140.84	0.0003	0.998	3.78	4.29	2.18	1.73
<i>C</i> <sub>0</sub> (mg/L)	Intraparticle diffusion model							
	<i>K</i> <sub>b</sub> (mg/g·min <sup>0.5</sup> )	<i>C</i> (mg/g)		<i>R</i> <sup>2</sup>				
10	2.63	1.35		0.999				
25	6.25	4.85		0.999				
50	12.1	13.9		0.998				
100	13.4	32.9		0.999				

steep increase in the first 60 min of adsorption, and after 90 min of adsorption, the slopes of these curves gradually level off until reaching equilibrium at 120 min. Clearly, the AB113 dye removal efficiency increases from 77.93% to 99.68% when the AB113 dye concentration is decreased from 100 mg/L to 10 mg/L. The decrease in the removal efficiency with an increasing initial AB113 concentration is because of the increase in the competition rate among AB113 molecules to occupy the available active sites of a fixed quantity of C-Fe<sub>2</sub>O<sub>3</sub>. In addition, the increase in the

AB113 dye concentration can lead to the rapid exhaustion of the used adsorbent; therefore, the adsorbent can become saturated [50]. On the other hand, Fig. 4c reveals that the AB113 removal efficiency is faster in the first 30 min, and the removal efficiency beyond 30 min is slightly slower. This result is because in the first 30 min of adsorption, the active adsorption sites on C-Fe<sub>2</sub>O<sub>3</sub> are easily available for AB113 dye molecules [51]. Afterward, the number of free sites decrease; hence, the AB113 dye removal efficiency is slightly slower, particularly after 60 min of adsorption.

**Fig. 5** Three stages of the kinetics adsorption of AB113 dye onto C-Fe<sub>2</sub>O<sub>3</sub>



## Interference Ions

Several studies have shown that different ions can interfere with the adsorption process by affecting the electrostatic interactions between the adsorbent and pollutant molecules [46, 47]. In fact, the reason for this phenomenon is that these ions have a higher ability to adsorb or neutralize the positive or negative charges on the adsorbent surface; thus, they inhibit the attraction between the pollutant molecules and adsorbent particles [52]. In the present study, the competition of NaCl, NaNO<sub>3</sub>, Na<sub>2</sub>CO<sub>3</sub>, and MgSO<sub>4</sub> ions on AB113 dye adsorption was investigated and compared with a control sample. This experiment was performed under the optimized conditions found from the previous analyses (pH 3, AB113 dye concentration = 10 mg/L, C-Fe<sub>2</sub>O<sub>3</sub> dose = 0.6 g/L, and adsorption time = 120 min), and the results are presented in Fig. 4d. In addition, the initial concentration of these interference ions was fixed at 10 mg/L. The presence of NaCl has the greatest impact on the AB113 dye removal efficiency. From this experiment, the effect of the presence of interference ions on the AB113 dye removal efficiency can be ranked as NaCl > NaNO<sub>3</sub> > MgSO<sub>4</sub> > Na<sub>2</sub>CO<sub>3</sub>.

## Kinetics Study

Analyses of the kinetic reaction are essential to evaluate the applicability of the used adsorbent, as it is useful for understanding the rate and type of adsorption (chemisorption, physisorption, or mixed). In addition, the determination of a kinetic model that can describe the experimental data of the kinetic reaction of an adsorbent–adsorbate system is necessary for the precise design of large-scale adsorption treatments [44, 53]. Therefore, the experimental data shown in Fig. 4c are first treated using Eq. 2 and then modeled with the pseudo-first-order (PFO) (Eq. 8) and pseudo-second-order (PSO) (Eq. 9) kinetic models [54, 55].

$$q_t = q_e (1 - \exp(-k_1 t)) \quad (8)$$

$$q_t = \frac{q_e^2 k_2 t}{1 + q_e k_2 t} \quad (9)$$

where  $K_1$  (1/min) and  $K_2$  (g/mg·min) are the PFO and PSO rate constants, respectively.

Nonlinear regression methodology using the MATLAB program was applied to model the kinetic data. Table 1 lists the results of the kinetic models and regression level parameters of AB113 dye adsorption onto C-Fe<sub>2</sub>O<sub>3</sub>. Note that the fitting of each kinetic model with the experimental data is estimated in accordance with the  $R^2$ ,  $SSE$ ,  $RMSE$ ,  $x^2$ , and  $ARE$  values as well as the convergence between the calculated uptake ( $q_e(cal)$ ) and experimental uptake ( $q_e(exp)$ ). The results show that high regression levels are obtained for the fitting of the PSO model compared to those for the fitting of the PFO model (Table 1). In addition, the values of  $q_e(cal)$  determined from the application of the PSO model are close to the  $q_e(exp)$  values. Therefore, the adsorption kinetics of the AB113 dye on C-Fe<sub>2</sub>O<sub>3</sub> follows PSO kinetics, suggesting a chemisorption process [35, 56].

By plotting the kinetics data according to the intraparticle diffusion model (IPD, Eq. 10), it is found that the kinetics adsorption of AB113 dye onto C-Fe<sub>2</sub>O<sub>3</sub> consists of three consecutive phases, as shown in Fig. 5: bulk diffusion, film diffusion, and pore diffusion. In fact, the first phase observed at  $3 < t^{0.5} < 5.5 \text{ min}^{0.5}$  represents the surface and IPD processes, the second phase observed at  $5.5 < t^{0.5} < 11 \text{ min}^{0.5}$  represents liquid film diffusion, and the third phase observed at  $11 < t^{0.5} < 17.5 \text{ min}^{0.5}$  represents the diffusion of AB113 dye molecules through pores to the active sites of C-Fe<sub>2</sub>O<sub>3</sub>; then, equilibrium conditions are achieved. In the present study, the first phase is modeled as a term in the IPD model. This is an important step in adsorption studies, as the IPD model provides information about the role of the IPD rate in controlling adsorption [47].

$$q_t = K_b t^{0.5} + C \quad (10)$$

**Table 2** Isotherm model parameters of AB113 dye adsorption on C-Fe<sub>2</sub>O<sub>3</sub> (conditions of this experiment were fixed at the following optimized values: pH 3; C-Fe<sub>2</sub>O<sub>3</sub> dose = 0.1–1 g/L; AB113 dye concentration = 10 mg/L; adsorption time = 120 min, and temperature = 25 ± 2 °C)

	Freundlich	Langmuir	Dubinin–Radushkevich	Temkin			
$K_F(\text{mg/g})(L/\text{mg})^{1/n}$	6.961	$Q_m(\text{mg/g})$	128.200	$q_m(\text{mg/g})$	58.710	$B(\text{J/mol})$	47.401
$1/n$	0.392	$R_L$	0.209	$\beta(\text{mol}^2/\text{kJ}^2)$	0.008	$K_T(\text{J/mol})$	19.411
$n$	2.551	$K_L(\text{L/mg})$	0.322	$E(\text{kJ/mol})$	7.491	$b(\text{L/g})$	52.260
$R^2$	0.994	$R^2$	0.941	$R^2$	0.674	$R^2$	0.839
$x^2$	2.920	$x^2$	4.714	$x^2$	11.650	$x^2$	4.762
$RMSE$	2.490	$RMSE$	3.961	$RMSE$	4.792	$RMSE$	9.890
$SSE$	1.843	$SSE$	6.721	$SSE$	9.460	$SSE$	14.811
$ARE$	2.080	$ARE$	4.340	$ARE$	10.380	$ARE$	19.371

where  $K_b$  ( $\text{mg/g}\cdot\text{min}^{0.5}$ ) is the rate constant of the IPD model and  $C$  ( $\text{mg/g}$ ) is the IPD constant that provides information about the thickness of the boundary layer.

The values of  $K_b$  and  $C$  represent the slope and intercept of the linear plot equation of the first phase in Fig. 5, respectively. The results show a high compatibility level ( $R^2 > 0.99$ ) of the AB113 dye kinetic data with the IPD model (Table 1). Therefore, it can be concluded that compared to other diffusion types, the IPD process is the dominant rate-controlling step during the adsorption of AB113 dye onto C-Fe<sub>2</sub>O<sub>3</sub>. This result is because the linear plot of  $q_t$  versus  $t^{1/2}$  does not pass through the origin; therefore, boundary layer diffusion occurs during the adsorption process. The positive values of  $C$  for all AB113 dye concentrations are indicative of involving the IPD in the adsorption process; nevertheless, the adsorption process is governed not only by IDP as the rate-limiting step but also by other factors controlling AB113 dye adsorption on C-Fe<sub>2</sub>O<sub>3</sub>.

### Adsorption Isotherms

To clarify the interaction between the adsorbent and target pollutant, adsorption isotherms, i.e., the Langmuir (Eq. 11), Freundlich (Eq. 12), Dubinin-Radushkevich (D-R, Eq. 13), and Temkin (Eq. 14) equations, were employed. The occurrence of adsorption in monolayers at homogeneous sites on the adsorbent is hypothesized by the Langmuir model. In contrast, the Freundlich isotherm describes adsorption on a heterogeneous surface and reversible adsorption [57]. Moreover, by the D-R model, the chemical or physical mechanism is appraised [58]. Through employment of the Temkin isotherm, the heat of adsorption and the adsorbent–adsorbate interaction are defined [59, 60].

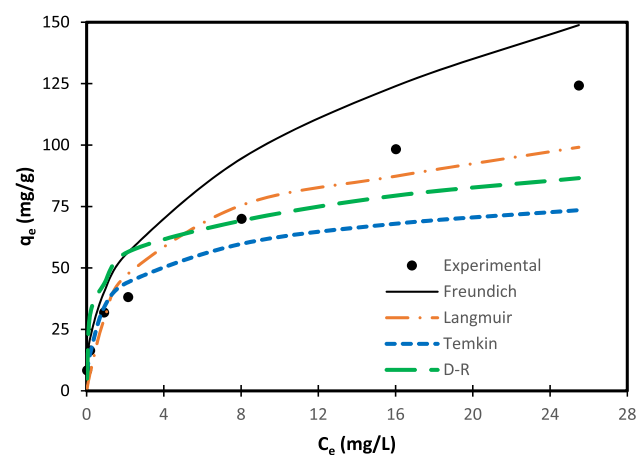


Fig. 6 Experimental and theoretical isothermal data of AB113 dye adsorption on C-Fe<sub>2</sub>O<sub>3</sub>

Table 3 Comparison between the maximum Langmuir adsorption capacities ( $Q_m$ ) of C-Fe<sub>2</sub>O<sub>3</sub> and of other adsorbents used for dyes removal

Adsorbents	Anionic dye	$Q_m(\text{mg/g})$	References
Multi-walled carbon nanotubes	Acid Blue 225	10.2	[52]
Cyperus rotundus	Acid Orang 7	31.98	[20]
Azolla filiculoides	Acid Blue 92	36.98	[37]
Orange bagasse	Reactive Blue 5	40.71	[54]
Hazelnut shell	Acid Blue 25	60.2	[59]
Jujuba seed	Congo Red	55.56	[55]
Canola	Acid Blue 113	56.9	[61]
Durian peel	Acid Green 25	63.29	[62]
Rice husk	Acid Red 66	65.1	[47]
Risk husk	Acid Blue 74	97.06	[60]
Pyracantha coccinea	Acid Red 44	105.1	[57]
Thuja orientalis cone	Acid Blue 40	114.9	[63]
Meal hull	Acid Blue 92	114.9	[58]
C-Fe <sub>2</sub> O <sub>3</sub>	Acid Blue 113	128.2	This study

$$q_e = \frac{Q_m K_L C_e}{1 + K_L C_e} \tag{11}$$

$$q_e = K_F C_e^{1/n} \tag{12}$$

$$q_e = q_m \exp(-\beta \epsilon^2) \tag{13}$$

$$q_e = B \ln(K_T C_e) \tag{14}$$

where  $Q_m$  ( $\text{mg/g}$ ) is a very important adsorption parameter in the Langmuir model, denoting the maximum  $q_t$  of the used adsorbent for the target pollutant;  $K_L$  ( $\text{L/mg}$ ) is an

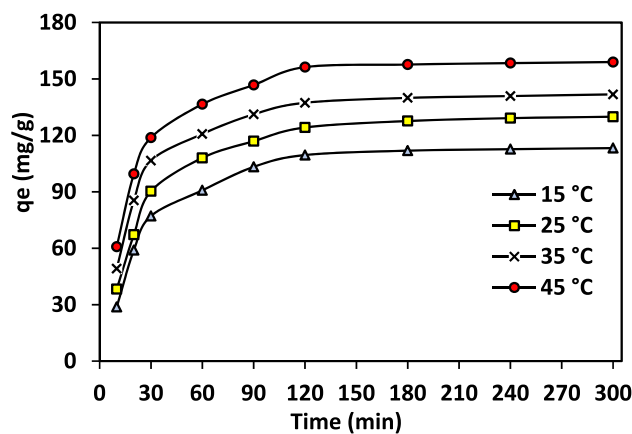


Fig. 7 Effects of temperature on the AB113 dye removal efficiency by C-Fe<sub>2</sub>O<sub>3</sub> (pH 3; C-Fe<sub>2</sub>O<sub>3</sub> dose=0.6 g/L; AB113 dye concentration = 10 mg/L; and adsorption time = 0–300 min)



**Table 4** Thermodynamic parameters for the adsorption process of AB113 dye on C-Fe<sub>2</sub>O<sub>3</sub>

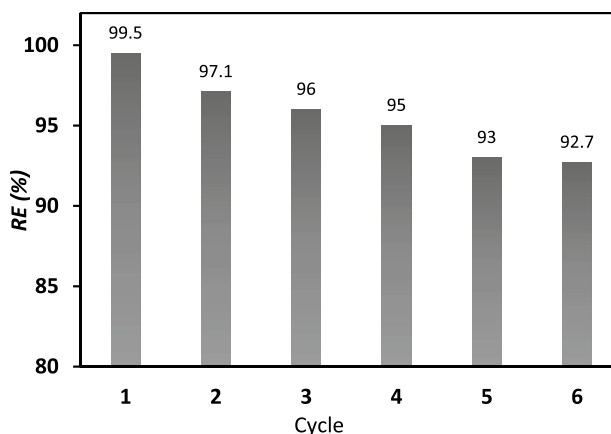
<i>T</i> (°C)	$\Delta G^\circ$ (kJ/mol)	$\Delta H^\circ$ (kJ/mol)	$\Delta S^\circ$ (kJ/mol·K)
15	− 2.78	50.20	0.182
25	− 3.92		
35	− 5.25		
45	− 8.51		

equilibrium constant reflecting the affinity level of the active sites of the adsorbent;  $K_F$  is the Freundlich constant, indicative of the binding energy (mg/g)(L/mg)<sup>1/*n*</sup>;  $\frac{1}{n}$  is the heterogeneity parameter;  $q_m$  is the theoretical adsorption capacity (mg/g) of the D-R model;  $\beta$  (mol<sup>2</sup>/kJ<sup>2</sup>) is the activity coefficient constant associated with the mean free sorption energy, which is denoted by  $E = \frac{1}{\sqrt{-2\beta}}$  (kJ/mol);  $\varepsilon = RT \ln \left( 1 + \frac{1}{C_e} \right)$  is the Polanyi potential (kJ/mol);  $K_T$  and  $B = \frac{RT}{b}$  are Temkin model constants that provide information about the heat of sorption (J/mol);  $b$  is the Temkin isotherm constant (L/g);  $R$  is the ideal gas constant (8.314 J/(mol·K)); and  $T$  is the thermodynamic absolute temperature (K).

In addition to the Langmuir model (Eq. 11), the characteristics of adsorption can be defined based on the dimensionless separation factor ( $R_L$ ) (Eq. 15). Based on the value of this factor, the favorable adsorption case can only be detected in the case of  $0 < R_L < 1$ .

$$R_L = \frac{1}{(1 + K_L C_0)} \quad (15)$$

Table 2 lists the determined values of the isotherm model parameters. The results show that the fitting parameters are high for the Freundlich model compared to those for the other isotherm models; thus, the isothermal data of AB113 dye adsorption on C-Fe<sub>2</sub>O<sub>3</sub> is consistent with the Freundlich model. This finding indicates that the AB113 dye molecules demonstrate multilayer adsorption at the heterogeneous adsorption sites of C-Fe<sub>2</sub>O<sub>3</sub>. In addition, as the value of the Freundlich parameter  $n$  is herein considered greater than one, the AB113 dye on the C-Fe<sub>2</sub>O<sub>3</sub> adsorption process is suitable [57]. The maximum adsorption capacity of AB113 dye by C-Fe<sub>2</sub>O<sub>3</sub> based on the fitting results of the Langmuir model is 128.2 mg/g. Furthermore, the value of the  $R_L$  parameter of the Langmuir model is between zero and one, indicating the favorable adsorption process of AB113 dye on C-Fe<sub>2</sub>O<sub>3</sub> [61]. Since the  $E$  obtained from the D–R isotherm is less than 8 kJ/mol, the adsorption of AB113 dye on C-Fe<sub>2</sub>O<sub>3</sub> is physical in nature. The theoretical models used for fitting the experimental isothermal data of AB113 dye adsorption on C-Fe<sub>2</sub>O<sub>3</sub> are graphically presented in Fig. 6.

**Fig. 8** Regeneration analysis of C-Fe<sub>2</sub>O<sub>3</sub> used for six consecutive AB113 dye adsorption–desorption cycles

Considering the results of the isotherm study, the adsorption capacity of C-Fe<sub>2</sub>O<sub>3</sub> was compared with that of other adsorbents in dye removal. As reported in Table 3, the adsorption capacity of C-Fe<sub>2</sub>O<sub>3</sub> is good and shows high adsorption compared to other adsorbents. Therefore, C-Fe<sub>2</sub>O<sub>3</sub> is more effective than other adsorbents for dye removal.

### Effect of Temperature and the Thermodynamic Study

The effect of temperature on the AB113 dye removal efficiency was examined in the range of 15–45 °C as a function of adsorption time (0–300 min), and the results are depicted in Fig. 7. This figure clarifies the positive effect of an increasing temperature on the removal efficiency of AB113 dye on C-Fe<sub>2</sub>O<sub>3</sub>. This behavior of improved removal efficiency with an increasing temperature is due to in the enhanced diffusion rate or kinetic energy of AB113 dye molecules across the bulk and internal boundary layers of the C-Fe<sub>2</sub>O<sub>3</sub> particle [56].

The thermodynamic parameters, including the enthalpy ( $\Delta H^\circ$ ) (kJ/mol), entropy ( $\Delta S^\circ$ ) (kJ/mol·K), and Gibbs free energy ( $\Delta G^\circ$ ) (kJ/mol), were calculated after determining the  $q_e$  values of the data in Fig. 7 using Eq. 2. The above three parameters were determined using Eqs. 16–18 [62, 64]. From these equations,  $\Delta H^\circ$  and  $\Delta S^\circ$  can be directly calculated from the linear plot of  $\ln K_o$  vs.  $1/T$ , where  $K_o$  (L/mg) is the equilibrium constant ( $= \frac{q_e}{C_e}$ ). The slope and intercept with the y-axis of the obtained trend line equation represent  $(-\Delta H^\circ/R)$  and  $(\Delta S^\circ/R)$ , respectively. Thereafter,  $\Delta G^\circ$  can be calculated using Eq. 18.

$$\Delta G^\circ = -RT(\ln K_o), \quad (16)$$

$$\ln K_o = \frac{\Delta S^\circ}{R} - \frac{\Delta H^\circ}{RT}, \quad (17)$$

$$\Delta G^\circ = \Delta H^\circ - T\Delta S^\circ, \quad (18)$$

Table 4 presents the results of the thermodynamic analysis. A positive  $\Delta S^\circ$  indicates the high randomness of AB113 dye adsorption and approves the stability of the adsorption process. The negative values of  $\Delta G^\circ$  suggest that the adsorption of AB113 dye on C-Fe<sub>2</sub>O<sub>3</sub> is a spontaneous reaction [65, 66]. Moreover, the increase in the negative values of  $\Delta G^\circ$  with an increase in temperature may be because of the dehydration phenomena of both adsorbent particles and pollutant molecules at high temperatures, which simplifies the reaction between them and ultimately makes the adsorption of AB113 dye on C-Fe<sub>2</sub>O<sub>3</sub> more favorable at high temperatures [67]. Furthermore, a positive  $\Delta H^\circ$  refers to the endothermic adsorption process of the AB113 dye on C-Fe<sub>2</sub>O<sub>3</sub>, which means the formation of strong chemical bonds between the adsorbed AB113 molecules and the C-Fe<sub>2</sub>O<sub>3</sub> surface [68].

### Regeneration Study

In the present study, the recyclability of C-Fe<sub>2</sub>O<sub>3</sub> was examined for six consecutive AB113 dye adsorption–desorption cycles under the following optimal conditions: pH 3; C-Fe<sub>2</sub>O<sub>3</sub> dose = 0.6 g/L; AB113 dye concentration = 10 mg/L; adsorption time = 120 min; and temperature = 25 ± 2 °C. The spent quantity of C-Fe<sub>2</sub>O<sub>3</sub> was separated from the aqueous solution using a magnet, rinsed with ethanol and deionized water, dried at 75 °C for 4 h, and then reused in the next AB113 dye adsorption cycle. The results of this experiment are presented in Fig. 8, revealing that C-Fe<sub>2</sub>O<sub>3</sub> can be recycled six times to adsorb AB113 dye. This figure also demonstrates that the removal efficiency of AB113 dye decreases by only 7% from the 1<sup>st</sup> to the 6<sup>th</sup> adsorption cycle. This decrease may be because of the loss of the adsorption ability of C-Fe<sub>2</sub>O<sub>3</sub> due to the washing process [69]. Based on these findings, it can be concluded that C-Fe<sub>2</sub>O<sub>3</sub> has an excellent shelf life for use in an AB113 dye adsorption treatment system.

### Conclusion

The current work represents the first study on the application of chitosan magnetized by Fe<sub>2</sub>O<sub>3</sub> nanoparticles (C-Fe<sub>2</sub>O<sub>3</sub>) for removing acid blue 113 (AB113) dye from aqueous solutions. Characterization analyses using advanced techniques, including SEM/EDX, TEM, XRD, FTIR, TGA, BET, and pH<sub>pzc</sub>, revealed that the adsorptive specifications of chitosan, such as the surface morphology, magnetization value, and thermal stability, were greatly improved after magnetization

with Fe<sub>2</sub>O<sub>3</sub> nanoparticles. In addition, the 2D and 3D AFM images evidenced the adsorption phenomenon of AB113 dye on C-Fe<sub>2</sub>O<sub>3</sub>. The AB113 dye removal efficiency was 99.68% and occurred under the following conditions: pH 3, C-Fe<sub>2</sub>O<sub>3</sub> dose = 0.6 g/L, AB113 dye concentration = 10 mg/L, and adsorption time = 120 min. The presence of interference ions, including NaCl, NaNO<sub>3</sub>, Na<sub>2</sub>CO<sub>3</sub>, and MgSO<sub>4</sub>, led to a negative effect on the AB113 dye removal efficiency but at different levels. The kinetic data obtained at different AB113 dye concentrations (10, 25, 50, and 100 mg/L) were consistent with the pseudo-second-order model. Based on the determined statistical goodness values of nonlinear fitting, the experimental data relevant to the isotherm and kinetic studies could be represented by the Freundlich and pseudo-second-order kinetic equations, respectively. In addition, the determined values of the thermodynamic parameters (positive  $\Delta H^\circ$  and  $\Delta S^\circ$  values and negative  $\Delta G^\circ$  values) indicated that the process of AB113 dye adsorption on C-Fe<sub>2</sub>O<sub>3</sub> was favorable, spontaneous, and endothermic. Compared with other adsorbents used for dye removal, it was shown that C-Fe<sub>2</sub>O<sub>3</sub> was an efficacious adsorbent and good alternative for treating wastewater containing AB113 dye in acidic media. Additionally, C-Fe<sub>2</sub>O<sub>3</sub> could be recycled for six consecutive AB113 dye adsorption–desorption cycles with little loss in its efficacy (7%). The key finding of this study was that C-Fe<sub>2</sub>O<sub>3</sub> has a high ability to remove AB113 dye from aqueous solutions; thus, it has potential for possible application in tertiary treatment units of dye effluents.

**Acknowledgements** The authors are grateful to the Zahedan University of Medical Sciences (Iran) for the laboratory assistance and financial support of this research.

### Declarations

**Conflict of interest** There are no conflicts of interest to declare.

### References

1. Wu P, Wu T, He W, Sun L, Li Y (2013) Adsorption properties of dodecylsulfate-intercalated layered double hydroxide for various dyes in water. *Colloids Surf A* 436:726–731
2. Samarghandi MR, Tari K, Shabanloo A, MehdiSalari M, Zolghadr NH (2020) Synergistic degradation of acid blue 113 dye in a thermally activated persulfate (TAP)/ZnO-GAC oxidation system: degradation pathway and application for real textile wastewater. *Sep Purif Technol* 247:116931
3. Shan R, Yan L, Yang Y, Yang K, Yu S, Yu H (2015) Highly efficient removal of three red dyes by adsorption onto Mg–Al-layered double hydroxide. *J Ind Eng Chem* 21:561–568
4. Bazrafshan E, Ahmadabadi A, Mahvi AH (2013) Reactive Red-120 removal by activated carbon obtained from cumin herb wastes. *Fresen Environ Bull* 22:584–590

5. Giustetto R, Wahyudi O (2011) Sorption of red dyes on palygorskite: synthesis and stability of red/purple Mayan nanocomposites. *Microporous Mesoporous Mater* 142:221–235
6. Crini G, Badot PM (2008) Application of chitosan, a natural aminopolysaccharide, for dye removal from aqueous solutions by adsorption processes using batch studies: a review of recent literature. *Prog Polym Sci* 33:399–447
7. Balarak D, Abasizdeh H, Jalalzayi Z, Rajiv P, Vanathi P (2020) Batch adsorption of acid blue 113 dye from aqueous solution using surfactant-modified zeolite. *Indian J Environ Prot* 40(9):927–933
8. Savic I, Gajic D, Stojiljkovic S, Savic I (2014) Modeling and optimization of methylene blue adsorption from aqueous solution using bentonite clay. *Comput Aided Chem Eng* 33:1417–1422
9. Zhang YJ, Liu LC, Ni LL, Wang BL (2013) A facile and low-cost synthesis of granulated blast furnace slag-based cementitious material coupled with  $\text{Fe}_2\text{O}_3$  catalyst for treatment of dye wastewater. *Appl Catal B* 138–139:9–16
10. Balarak D, Al-Musawi TJ, Mohammed IA, Abasizadeh H (2020) The eradication of reactive black 5 dye liquid wastes using *Azolla filiculoides* aquatic fern as a good and an economical biosorption agent. *SN Appl Sci* 2(6):1015
11. Asgari G, Shabanloo A, Salari M, Eslami F (2020) Sonophotocatalytic treatment of AB113 dye and real textile wastewater using  $\text{ZnO}$ /persulfate: Modeling by response surface methodology and artificial neural network. *Environ Res* 184:109367
12. Eren E (2010) Adsorption performance and mechanism in binding of azo dye by raw bentonite. *Clean Soil Air Water* 38:758–763
13. Sanghi R, Verma P (2013) Decolorisation of aqueous dye solutions by low-cost adsorbents: a review. *Color Technol* 129:85–108
14. Ma J, Cui B, Dai J, Li D (2011) Mechanism of adsorption of anionic dye from aqueous solutions onto organobentonite. *J Hazard Mater* 186:1758–1765
15. Li Q, Yue QY, Su Y, Gao BY, Sun HJ (2010) Equilibrium, thermodynamics and process design to minimize adsorbent amount for the adsorption of acid dyes onto cationic polymer-loaded bentonite. *Chem Eng J* 158:489–497
16. Hao Y, Yan L, Yu H, Yang K, Yu S, Shan RL (2014) Comparative study on adsorption of basic and acid dyes by hydroxy-aluminum pillared bentonite. *J Mol Liq* 199:202–207
17. Balarak D, Abasizadeh H, Yang JK, Shim MJ, Lee SM (2020) Biosorption of acid orange 7 (AO7) dye by canola waste: equilibrium, kinetic and thermodynamics studies. *Desal Water Treat* 190:331–339
18. Elgin AB, Özdemir O, Turan M, Turan AZ (2008) Color removal from textile dye bath effluents in a zeolite fixed bed reactor: determination of optimum process conditions using Taguchi method. *J Hazard Mater* 159:348–353
19. Sillanpää M, Mahvi AH (2021) Adsorption of Acid orange 7 dyes from aqueous solution using Polypyrrole/nanosilica composite: experimental and modelling. *Int J Environ Anal Chem*. <https://doi.org/10.1080/03067319.2020.1855338>
20. Balarak D, Azarpira H (2016) Biosorption of Acid Orange 7 using dried *Cyperus Rotundus*: isotherm studies and error functions. *Int J ChemTech Res* 9:543–549
21. Cheung WH, Szeto YS, McKay G (2007) Intraparticle diffusion processes during acid dye adsorption onto chitosan. *Bioresour Technol* 98:2897–2904
22. Xua L, Wang J (2012) Fenton-like degradation of 2, 4-dichlorophenol using  $\text{Fe}_3\text{O}_4$  magnetic nanoparticles. *Appl Catal B* 123–124:117–126
23. Kyzas GZ, Deliyanni EA (2013) Mercury(II) removal with modified magnetic chitosan adsorbents. *Molecules* 18:6193–6214
24. Bouatay F, Meksi N, Adeel S, Salah F, Mhenni F (2016) Dyeing behavior of the cellulosic and jute fibers with cationic dyes: process development and optimization using statistical analysis. *J Nat Fiber* 13:423–436
25. Mittal H, Mishra SB (2014) Gum ghatti and  $\text{Fe}_3\text{O}_4$  magnetic nanoparticles based nanocomposites for the effective adsorption of rhodamine B. *Carbohydr Polym* 101:1255–1264
26. Kavitha AL, Prabu HG, Babu SA (2012) Synthesis of low-cost Iron Oxide-Chitosan nanocomposite for antibacterial activity. *Int J Polym Mater Polym Biomat* 62:45–49
27. Tabak A, Baltas N, Afsin B, Emirik M, Caglar B, Eren E (2010) Adsorption of Reactive Red 120 from aqueous solutions by cetylpyridinium-bentonite. *J Chem Technol Biotechnol* 85:1199–1207
28. Gupta AK, Gupta M (2005) Synthesis and surface engineering of iron oxide nanoparticles for biomedical applications. *Biomaterials* 26:3995–4021
29. Khandanlou R, Ahmad MB, Shameli K, Kalantari K (2013) Synthesis and characterization of Rice straw/ $\text{Fe}_3\text{O}_4$  nanocomposite by a quick precipitation method. *Molecules* 18:6597–6607
30. Sun X, Peng B, Ji Y, Chen J, Li D (2009) Chitosan(chitin)/cellulose composite biosorbents prepared using ionic liquid for heavy metal ions adsorption. *AIChE* 55:2062–2069
31. Chokami MK, Babaei L, Zamani AA, Parizanganeh AH, Piri F (2017) Synthesized chitosan/iron oxide nanocomposite and shrimp shell in removal of nickel, cadmium and lead from aqueous solution. *Glob J Environ Sci Manage* 3(3):267–278
32. Broujeni B, Nilchi A, Hassani AH, Saberi R (2018) Preparation and characterization of chitosan/ $\text{Fe}_2\text{O}_3$  nano composite for the adsorption of thorium (IV) ion from aqueous solution. *Water Sci Technol* 78:708–720
33. Rahmani A, Salari M, Tari K, Shabanloo A, Shabanloo N, Bajalan S (2020) Enhanced degradation of furfural by heat-activated persulfate/nZVI-rGO oxidation system: degradation pathway and improving the biodegradability of oil refinery wastewater. *J Environ Chem Eng* 8:104468
34. Rahmani A, Mohammadi AM, Leili M, Shabanloo A, Ansari A, Alizadeh S, Nematollahi D (2021) Electrocatalytic degradation of diuron herbicide using three-dimensional carbon felt/ $\beta\text{-PbO}_2$  anode as a highly porous electrode: influencing factors and degradation mechanisms. *Chemosphere* 276:130141
35. Khodadadi M, Al-Musawi TJ, Kamranifar M, Saghi MH, Panahi AH (2019) A comparative study of using barberry stem powder and ash as adsorbents for adsorption of humic acid. *Environ Sci Pollut Res* 26:26159–26169
36. Alwared AI, Al-Musawi TJ, Muhaisn LF, Mohammed AA (2021) The biosorption of reactive red dye onto orange peel waste: a study on the isotherm and kinetic processes and sensitivity analysis using the artificial neural network approach. *Environ Sci Pollut Res* 28(3):2848–2859
37. Balarak D, Mahdavi Y, Bazrafshan E, Mahvi AH (2016) Kinetic, isotherms and thermodynamic modeling for adsorption of acid blue 92 from aqueous solution by modified *azolla filiculoides*. *Fresen Environ Bull* 25(5):1321–1330
38. Hu Z, Chen H, Ji F (2015) Removal of Congo red from aqueous solution by cattail root. *J Hazard Mater* 173:292–297
39. Fontana KB, Chaves ES, Sanchez JDS, Lenzi GG (2016) Textile dye removal from aqueous solutions by malt bagasse: isotherm, kinetic and thermodynamic studies. *Ecotoxicol Environ Saf* 124:329–336
40. Hilal NM, Ahmed IA, Badr EE (2012) Removal of acid dye (AR37) by adsorption onto potatoes and egg husk: a comparative study. *J American Sci* 8:341–348
41. Rahmani AR, Salari M, Shabanloo A, Shabanloo N, Bajalan S, Vaziri Y (2020) Sono-catalytic activation of persulfate by nZVI-reduced graphene oxide for degradation of nonylphenol in aqueous solution: process optimization, synergistic effect and degradation pathway. *J Environ Chem Eng* 8:104202
42. Shabanloo M, Salari M, Shabanloo N, Dehghanib MH, Pittman CU, Mohane D (2020) Heterogeneous persulfate activation by

- nano-sized  $Mn_3O_4$  to degrade furfural from wastewater. *J. Mol. Liq.* 298:112088
43. Nasseh N, Khosravi R, Rumman GA, Ghadirian M, Eslami H, Khoshnamvand M, Al-Musawi TJ, Khosravi A (2021) Adsorption of Cr(VI) ions onto powdered activated carbon synthesized from *Peganum harmala* seeds by ultrasonic waves activation. *Environ Technol Innov* 21:101277
  44. Al-Musawi TJ, Brouers F, Zarrabi M (2018) What can the use of well-defined statistical functions of pollutants sorption kinetics teach us? A case study of cyanide sorption onto LTA zeolite nanoparticles. *Environ Technol Innov* 10:46–54
  45. Rostamian R, Behnejad H (2016) A comparative adsorption study of sulfamethoxazole onto graphene and graphene oxide nanosheets through equilibrium, kinetic and thermodynamic modeling. *Process Saf Environ Prot* 102:20–29
  46. Samarghandi M, Al-Musawi T, Mohseni-Bandpi A, Zarrabi M (2015) Adsorption of cephalixin from aqueous solution using natural zeolite and zeolite coated with manganese oxide nanoparticles. *J Mo Liq* 211:431–441
  47. Balarak D, Mostafapour FK (2018) Adsorption of acid red 66 dye from aqueous solution by heat-treated rice husk. *Res J Chem Environ* 22(12):80–84
  48. Dotto GL, Pinto LAA (2011) Adsorption of food dyes acid blue 9 and yellow 3 onto chitosan: stirring rate effect in kinetics and mechanism. *J Hazard Mater* 187:164–170
  49. Yao Y, Xu F, Chen M, Xu Z, Zhu Z (2010) Adsorption behavior of methylene blue on carbon nanotubes. *Bioresour Technol* 101:3040–3046
  50. Joshi S, Garg V, Kataria N, Kadirvelu K (2019) Applications of  $Fe_3O_4@AC$  nanoparticle for dye removal from simulated wastewater. *Chemosphere*. 236:124280
  51. Madrakian T, Afkhami A, Ahmadi M, Bagheri H (2011) Removal of some cationic dyes from aqueous solutions using magnetic-modified multi-walled carbon nanotubes. *J Hazard Mater* 196:109–114
  52. Balarak D, Mostafapour FK, Joghataei A (2016) Adsorption of: Acid Blue 225 dye by Multi Walled Carbon Nanotubes: Determination of equilibrium and kinetics parameters. *Pharm Chem* 8:138–145
  53. Mustafa YA, Jaid GM, Alwared AI, Ebrahim M (2014) The use of artificial neural network (ANN) for the prediction and simulation of oil degradation in wastewater by AOP. *Environ Sci Pollut Res* 21:7530–7537
  54. Fiorentin LD, Trigueros DEG, Pereira NC, Barros STD, Santos OAA (2010) Biosorption of reactive blue 5G dye onto drying orange bagasse in batch system: kinetic and equilibrium modeling. *Chem Eng J* 163:68–77
  55. Somasekhara R, Sivaramakrishna MC, Varada R (2012) The use of an agricultural waste material, Jujuba seeds for the removal of anionic dye (Congo red) from aqueous medium. *J Hazard Mater* 203–204:118–127
  56. Mohammed AA, Najim AA, Al-Musawi TJ, Alwared AI (2019) Adsorptive performance of a mixture of three nonliving algae classes for nickel remediation in synthesized wastewater. *J Environ Health Sci Eng* 17:529–538
  57. Akar T, Celik S, Akar ST (2010) Biosorption performance of surface modified biomass obtained from *Pyracantha coccinea* for the decolorization of dye contaminated solutions. *Chem Eng J* 160:466–472
  58. Arami M, Limaee NY, Mahmoodi NM, Tabrizi NS (2006) Equilibrium and kinetics studies for the adsorption of direct and acid dyes from aqueous solution by soy meal hull. *J Hazard Mater* 135:171–179
  59. Ferrero F (2007) Dye removal by low cost adsorbents: hazelnut shells in comparison with wood sawdust. *J Hazard Mater* 142:144–152
  60. Lakshmi UR, Srivastava VC, Mall ID, Lataye DH (2009) Rice husk ash as an effective adsorbent: evaluation of adsorptive characteristics for Indigo Carmine dye. *J Environ Manag* 90:710–720
  61. Zazouli MA, Ebrahimi CJY, M, Mahdavi Y. (2013) Investigating the removal rate of acid blue 113 from aqueous solution by canola (*Brassica Napus*). *J Mazand Univ Med Sci* 22:70–78
  62. Hameed BH, Hakimi H (2008) Utilization of durian (*Durio zibethinus Murray*) peel as low cost sorbent for the removal of acid dye from aqueous solutions. *Biochem Eng J* 39:338–343
  63. Akar T, Ozcan AS, Tunali S, Ozcan A (2008) Biosorption of a textile dye (Acid Blue 40) by cone biomass of *Thuja orientalis*: estimation of equilibrium, thermodynamic and kinetic parameters. *Bioresour Technol* 99:3057–3065
  64. Meziti C, Boukerroui A (2012) Removal of a Basic Textile Dye from Aqueous Solution by Adsorption on Regenerated Clay. *Procedia Engineering* 33:303–312
  65. Chu HC, Lin LH, Liu HJ, Chen KM (2013) Utilization of dried activated sludge for the removal of basic dye from aqueous solution. *Desal Wat Treat* 51:7074–7080
  66. Han R, Zhang J, Han P, Wang Y (2009) Study of equilibrium, kinetic and thermodynamic parameters about methylene blue adsorption onto natural zeolite. *Chem Eng J* 145:496–504
  67. Gok O, Ozcan AS, Ozcan A (2010) Adsorption behavior of a textile dye of Reactive Blue 19 from aqueous solutions onto modified bentonite. *Appl Surf Sci* 256:5439–5443
  68. Suna D, Zhanga X, Wub Y, Liu X (2010) Adsorption of anionic dyes from aqueous solution on fly ash. *J Hazard Mater* 181:335–342
  69. Osma JF, Saravia V, Toca-Herrera JL, Couto SR (2007) Sunflower seed shells: a novel and effective low-cost adsorbent for the removal of the diazo dye Reactive Black 5 from aqueous solutions. *J Hazard Mater* 147:900–905

**Publisher's Note** Springer Nature remains neutral with regard to jurisdictional claims in published maps and institutional affiliations.